Scattering and absorption of light by near-Earth-object surfaces: photometric and polarimetric phase effects

Karri Muinonen
Academy Professor
Department of Physics, University of Helsinki, Helsinki, Finland

Acknowledgments: Research Council of Finland, European Research Council

EU-ESA Near-Earth-Object Workshop, ESOC, Darmstadt, Germany, November 11-13, 2024

"… how the *H* magnitude is currently determined from observations,
how the different physical characterisation techniques are used to determine the albedo,
and the different techniques directly used to determine the object size …"

Contents

Introduction

- Physical characterization of airless Solar System objects at large
- Forward and inverse scattering problems concerning regolith and particle physical properties
- Plane of scattering, scattering angle, solar phase angle
- Disk-integrated brightness *L* (in magnitude scale $-2.5 \log_{10} L$)
- Degree of linear polarization
  $P_r = (L_r - L_l)/(L_r + L_l)$
- Size (*D*, km), geometric albedo (p_V), and absolute magnitude (*H*, mag)

$$D = \frac{1329 \times 10^{-0.2H}}{\sqrt{p_V}}$$

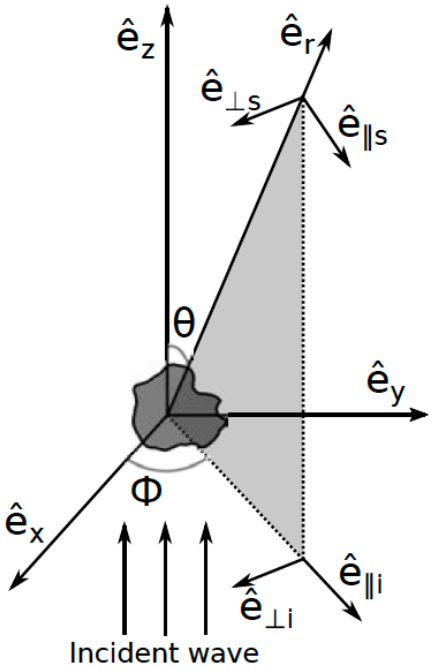

Figure 2.2: Illustration of the incident wave and the scattering plane. (Bohren and Huffman, 1983)

Väisänen, Ph.D. thesis, 2020

Polarimetric & photometric observations

Moon

Photometry

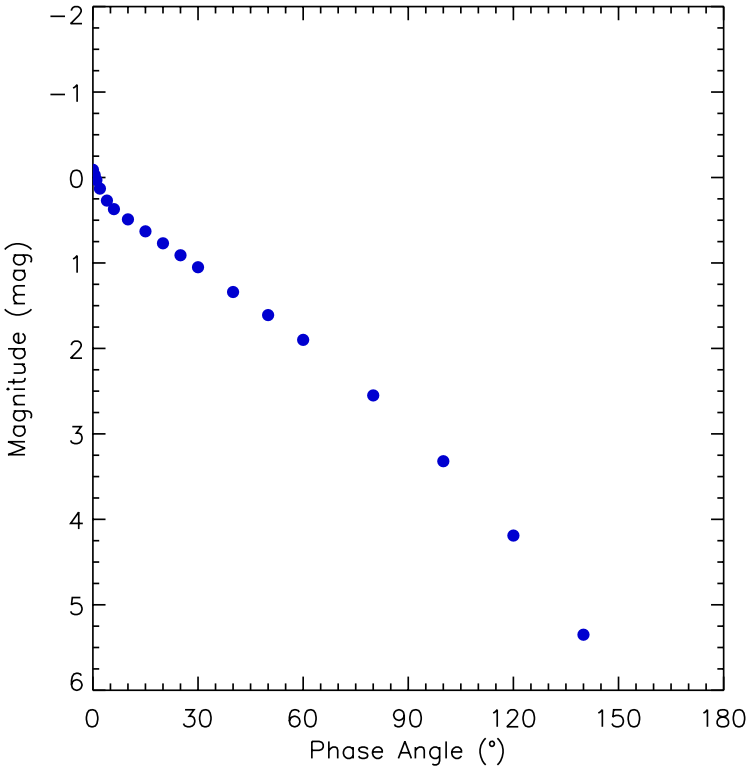

Polarimetry

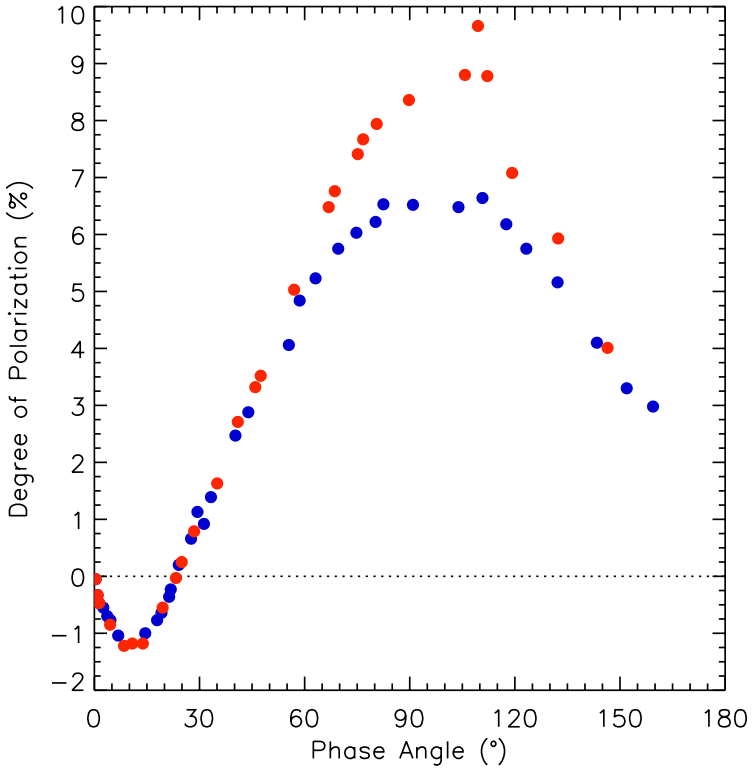

Spherical albedo $A = pq$,
$A \approx 0.1$?

Phase integral
$q \approx 0.4\text{-}0.5$?

Geometric albedo
$p \approx 0.1\text{-}0.2$?

NEOs vs. Moon ?

Rougier (1933), Lyot (1929)

Asteroids

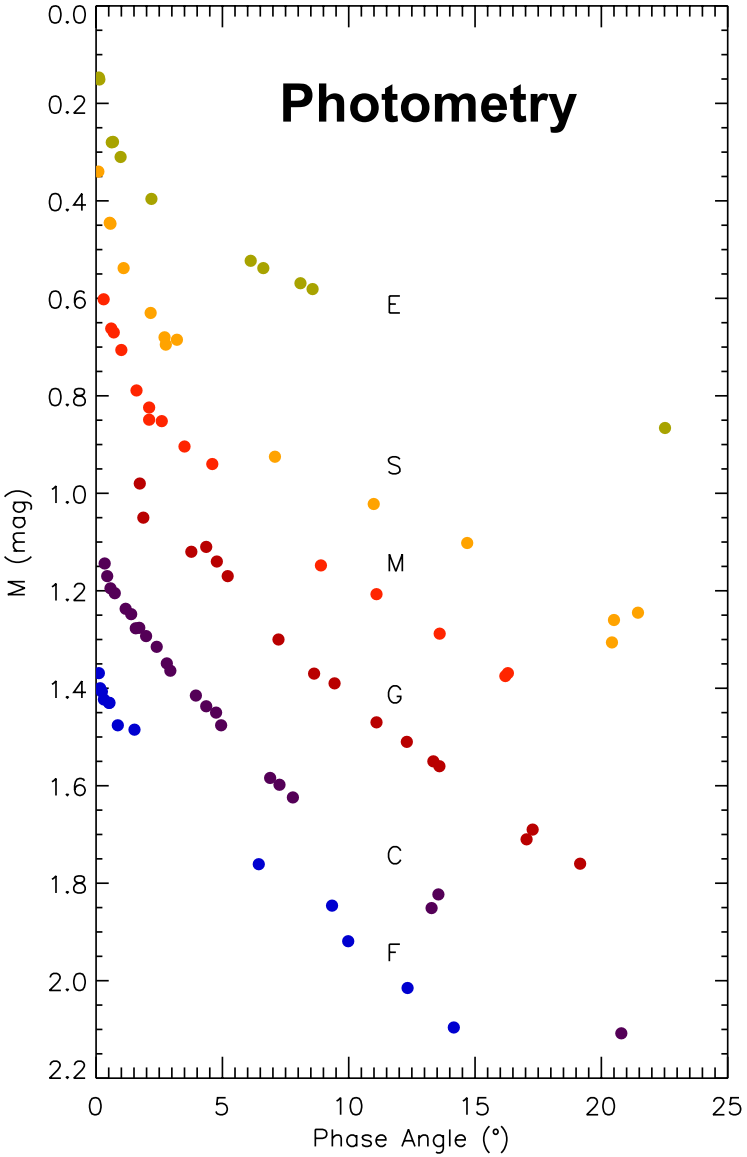

Muinonen et al., in Polarimetry of Stars and Planetary Systems, 2016 (obs. ref. therein)

Cellino et al. 2006, Gil-Hutton et al. 2008, Frattin et al. 2022: Spinel-rich “Barbarian” asteroids, (234) Barbara, inversion angle at ~30 deg

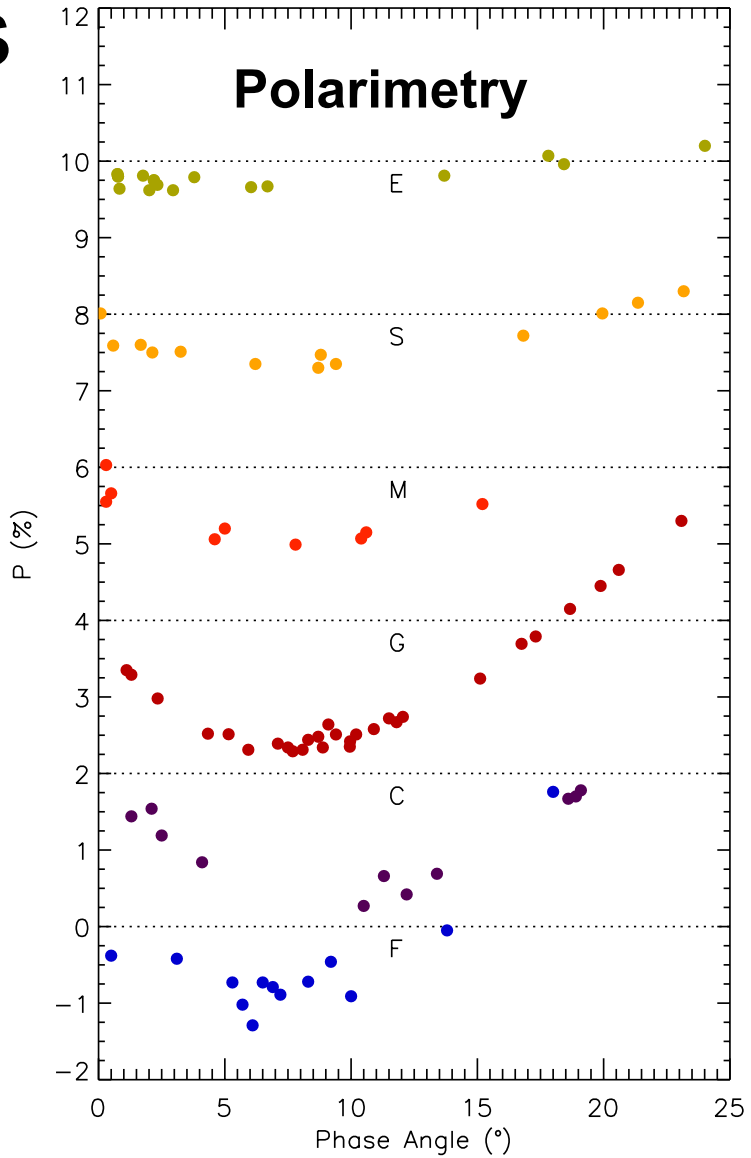

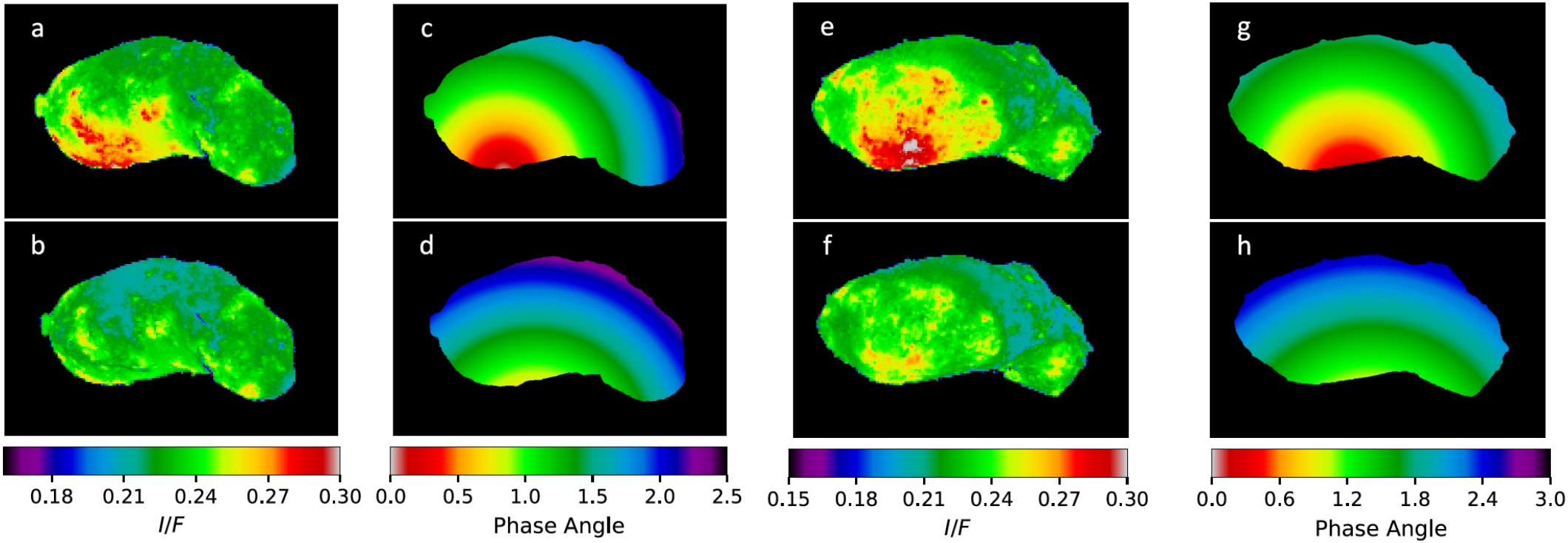

Fig. 3. *Panels a and b*: I/F maps of Set 1. *Panels c and d*: phase angle maps for the corresponding I/F maps. The opposition is located at the bottom of these maps. The reddish parts in the *top left* map correspond to a high-albedo region that is close to the opposition. *Panels e and f*: I/F maps of Set 2. *Panels g and h*: phase angle maps for the corresponding I/F maps. The opposition is located at the bottom of these maps.

Opposition effect on asteroid (25143) Itokawa, Lee & Ishiguro, A&A 2018

DART impact on Didymos-Dimorphos system

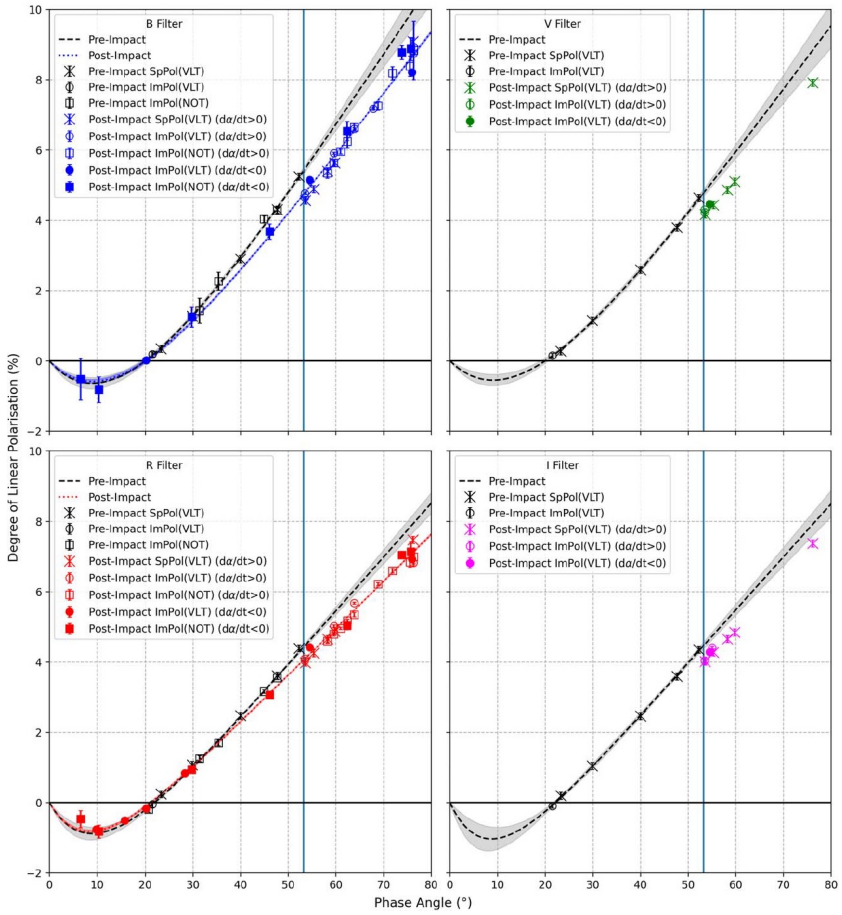

Figure 2. The polarimetric phase curves of Didymos–Dimorphos in the *BVRI* filters. The vertical blue line indicates the phase angle of the asteroid system at the time of the DART impact (∼53.2°). The SpPol data points refer to the spectropolarimetric measurements taken with the VLT by Bagnulo et al. (2023), while the ImPol data points refer to the imaging (aperture) polarimetric measurements taken with the VLT and NOT (this study). In each plot, the black symbols and curve represent pre-impact measurements and their best fit, while the colored symbols and curve represent post-impact measurements and fit. The shaded area around the curves (where applicable) represents 1σ of the fit. In the case of the ImPol measurements, the open and filled data points are measurements taken when the phase angle was increasing ($d\alpha/dt > 0$) and decreasing ($d\alpha/dt < 0$, after α peak at 76.34° on 2022 October 21), respectively.

- ESO VLT/FORS2 and NOT polarimetry by Bagnulo et al. (2023) and Gray et al. (2024), modeling by Penttilä et al. (2024)

Coherent backscattering mechanism (CBM)

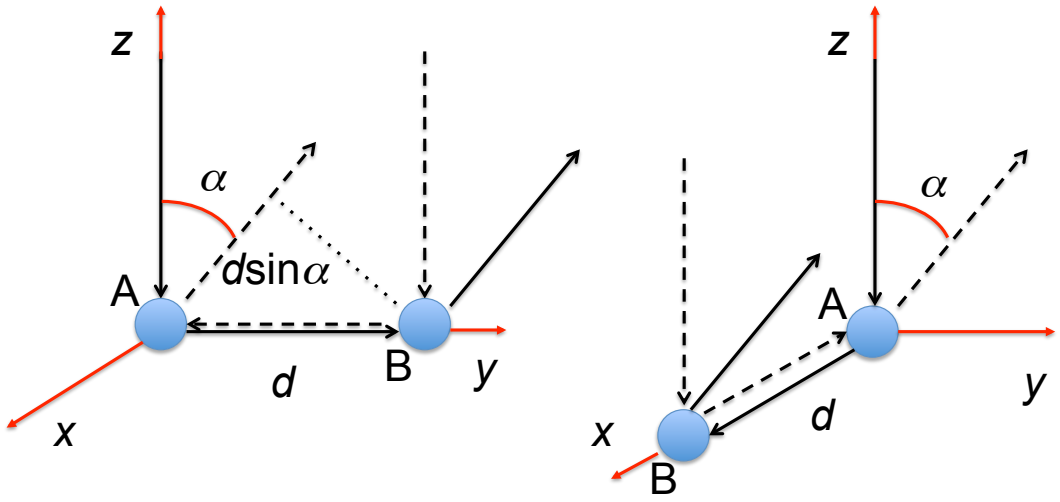

Muinonen (1989, 1990)
Shkuratov (1985, 1988, 1989)

Shadowing mechanism (SM)

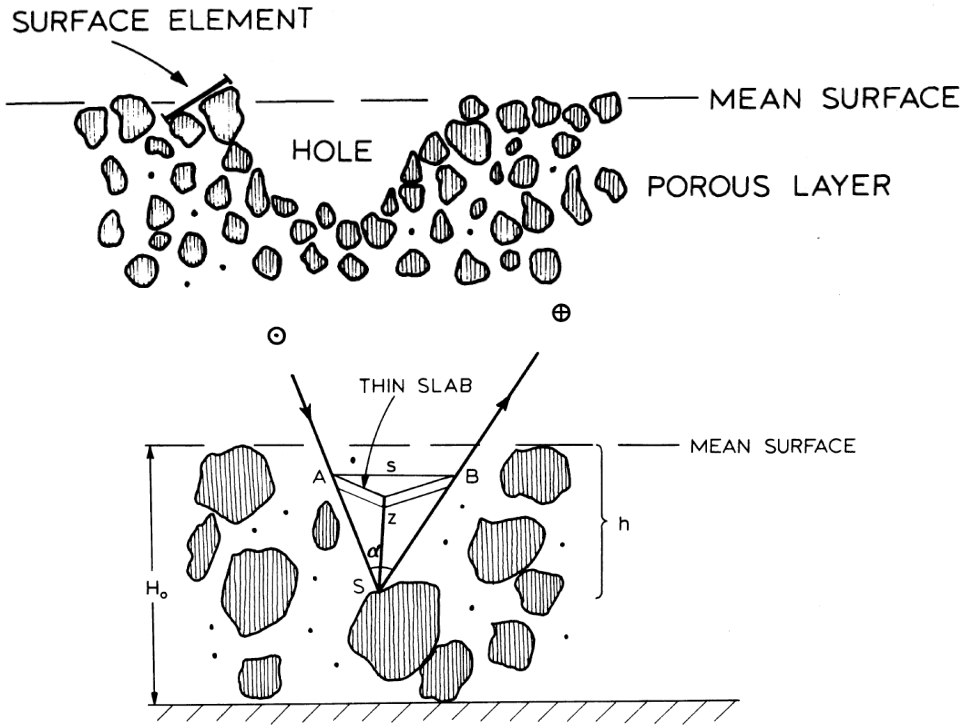

e.g., Lumme & Bowell (1981), Hapke (1963), Seeliger (1887), Russell (1916)

Single-particle mechanism (SPM)

Feldspar samples from Granada-Amsterdam Light Scattering Database (Volten et al. 2001, Muñoz et al. 2012)

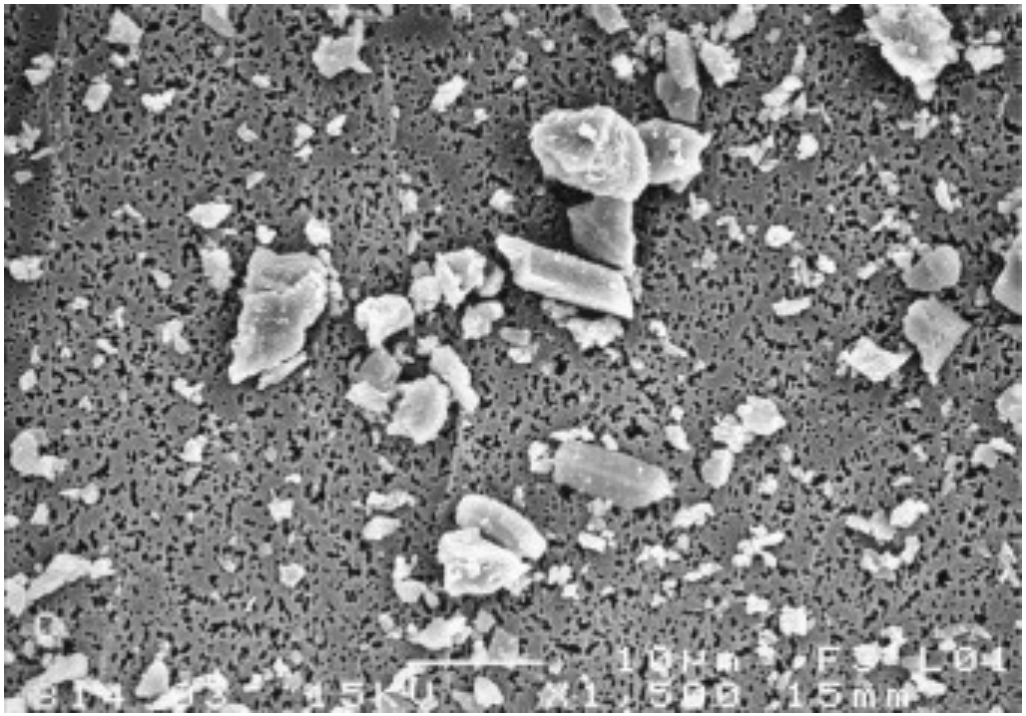

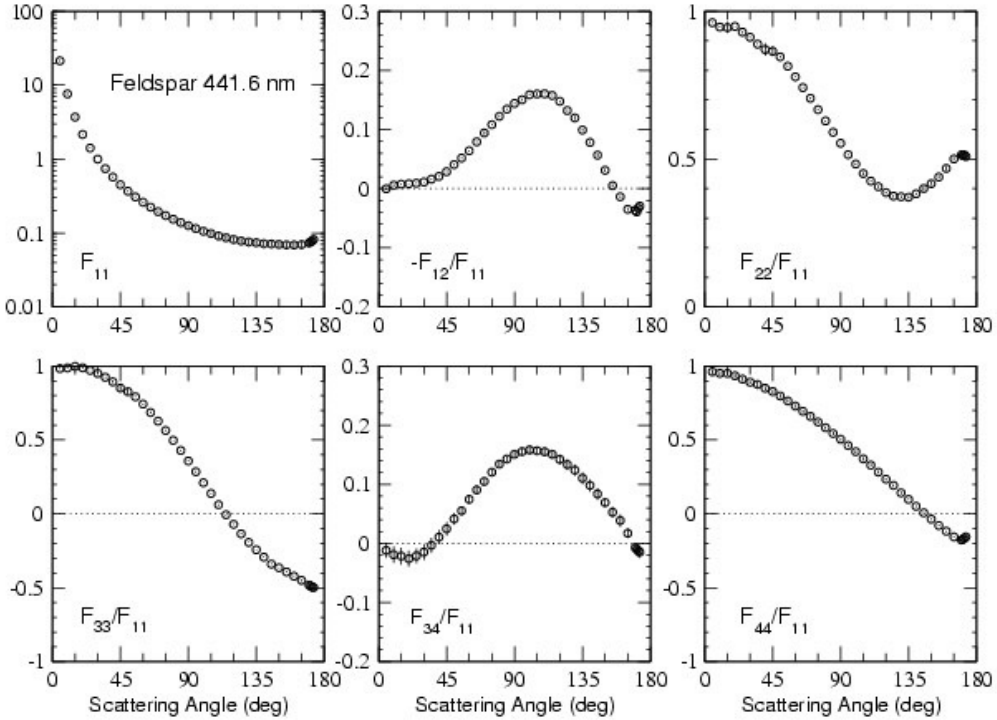

SPM can be explained with the help of standing electromagnetic waves induced inside the particles (Muinonen et al. 2011)

Theory and numerical methods

- Maxwell equations & Radiative transfer equation
- Radiative transfer and coherent backscattering (RT-CB; Muinonen et al., ApJ 2012; Muinonen, WRM 2004 and URSI EMTS 1989)
- Superposition *T*-Matrix Method (STMM or MSTM; Mackowski & Mishchenko, JQSRT 2011; FaSTMM, Markkanen & Yuffa JQSRT 2017)
- Electric Current Volume Integral Equation Method (JVIE; Markkanen & Yuffa, JQSRT 2017, Markkanen et al., IEEE-TAP 2012)
- Radiative transfer with reciprocal transactions (R^2T^2; Muinonen et al., URSI EMTS 2016ab, RS 2017, OL 2018, JoVE 2019; Markkanen et al., OL 2018, Markkanen et al., ApJ 2018, Väisänen et al., PLoS ONE 2019, OL 2020)
- RT-CB for nonspherical particles using decomposition of ensemble-averaged scattering matrices into pure Mueller matrices (Muinonen & Penttilä 2024, Muinonen et al., 2024)

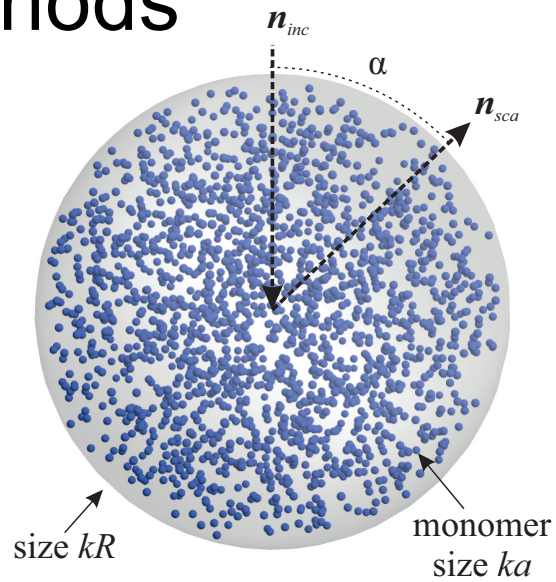

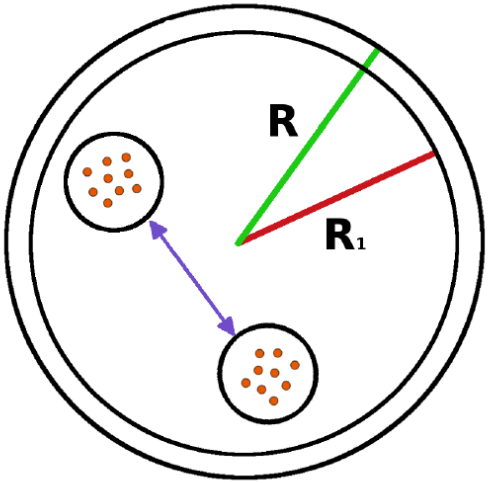

Scattering matrix decomposition

Ensemble-averaged scattering phase matrix:

$$\mathbf{P_0} = \begin{pmatrix} P_{11}^{(0)} & P_{12}^{(0)} & 0 & 0 \\ P_{21}^{(0)} & P_{22}^{(0)} & 0 & 0 \\ 0 & 0 & P_{33}^{(0)} & P_{34}^{(0)} \\ 0 & 0 & P_{43}^{(0)} & P_{44}^{(0)} \end{pmatrix}$$

$$P_{21}^{(0)} = P_{12}^{(0)},$$

$$P_{43}^{(0)} = -P_{34}^{(0)}.$$

(Empirical model in preparation.)

Decomposition into pure Mueller matrices for RT-CB:

$$\mathbf{P} = w_U\,\mathbf{U} + w_V\,\mathbf{V} + w_W\,\mathbf{W} + w_Z\,\mathbf{Z},$$

$$0 \le w_U \le 1, \quad 0 \le w_V \le 1, \quad 0 \le w_W \le 1, \quad 0 \le w_Z \le 1,$$

$$w_U + w_V + w_W + w_Z = 1,$$

$$\mathbf{U} = \begin{pmatrix} U_{11} & U_{12} & 0 & 0 \\ U_{12} & U_{11} & 0 & 0 \\ 0 & 0 & U_{33} & U_{34} \\ 0 & 0 & -U_{34} & U_{33} \end{pmatrix}, \quad \mathbf{W} = \begin{pmatrix} W_{11} & 0 & 0 & 0 \\ 0 & -W_{11} & 0 & 0 \\ 0 & 0 & -W_{11} & 0 \\ 0 & 0 & 0 & W_{11} \end{pmatrix},$$

$$\mathbf{V} = \begin{pmatrix} V_{11} & V_{12} & 0 & 0 \\ V_{12} & V_{11} & 0 & 0 \\ 0 & 0 & V_{33} & V_{34} \\ 0 & 0 & -V_{34} & V_{33} \end{pmatrix}, \quad \mathbf{Z} = \begin{pmatrix} Z_{11} & 0 & 0 & 0 \\ 0 & -Z_{11} & 0 & 0 \\ 0 & 0 & Z_{11} & 0 \\ 0 & 0 & 0 & -Z_{11} \end{pmatrix},$$

Validation of numerical methods:

Discrete media of spherical particles

- R^2T^2, exact incoherent interactions using *T*-matrices from FaSTMM (Muinonen et al., OL 2018)
- Spherical media, radius $kR = 100$:
  - Number of spheres $N = 31250$
  - Case, Ice:
    - radius $kr = 2.0$, refractive index $m = 1.31$
    - single-scattering albedo $\omega = 1.0$
    - volume densities $v = 0.25$
- For RT-CB with decomposition, see Muinonen et al. (JQSRT 2024)

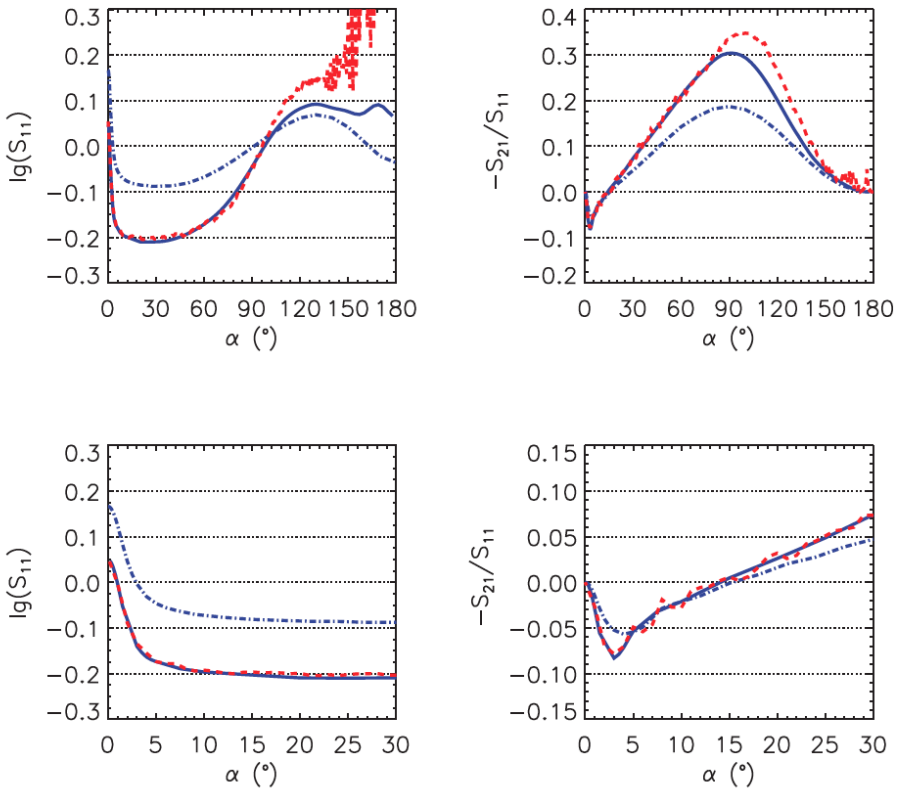

Discrete media of nonspherical particles

- R^2T^2, exact incoherent interactions using *T*-matrices from JVIE (Markkanen et al., Optics Letters 2018)
- Spherical media, radius $kR = 60$, Voronoi media:
  - Case, Ice:
    - radius $kr = 2.0$, refractive index $m = 1.31$
    - volume densities $v = 0.125, 0.25$

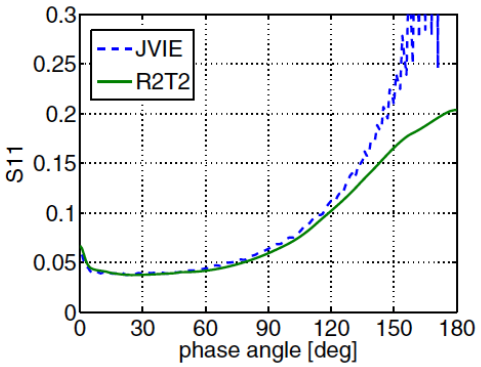

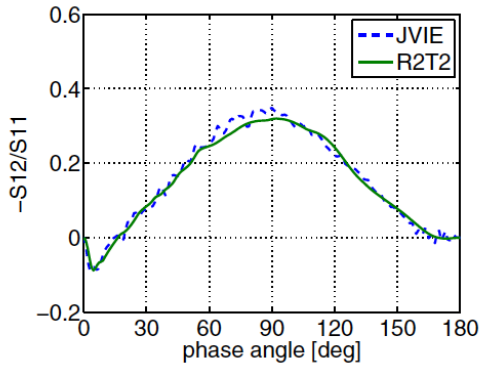

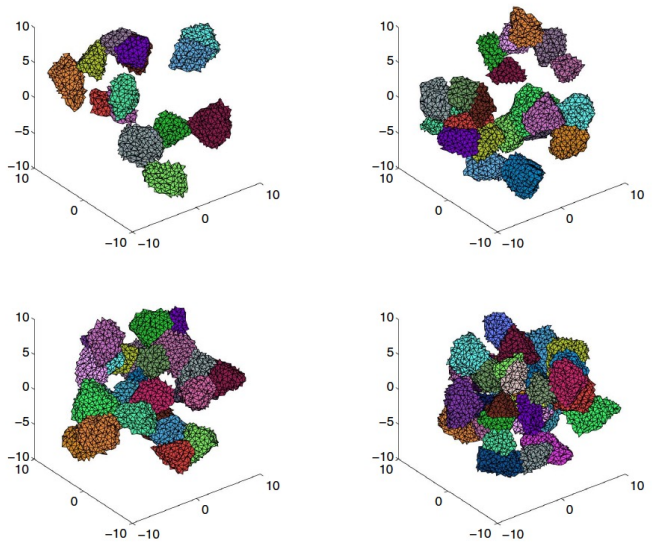

Cosmic Dust Laboratory scattering measurements (CoDuLab, Olga Munoz et al. 2012)

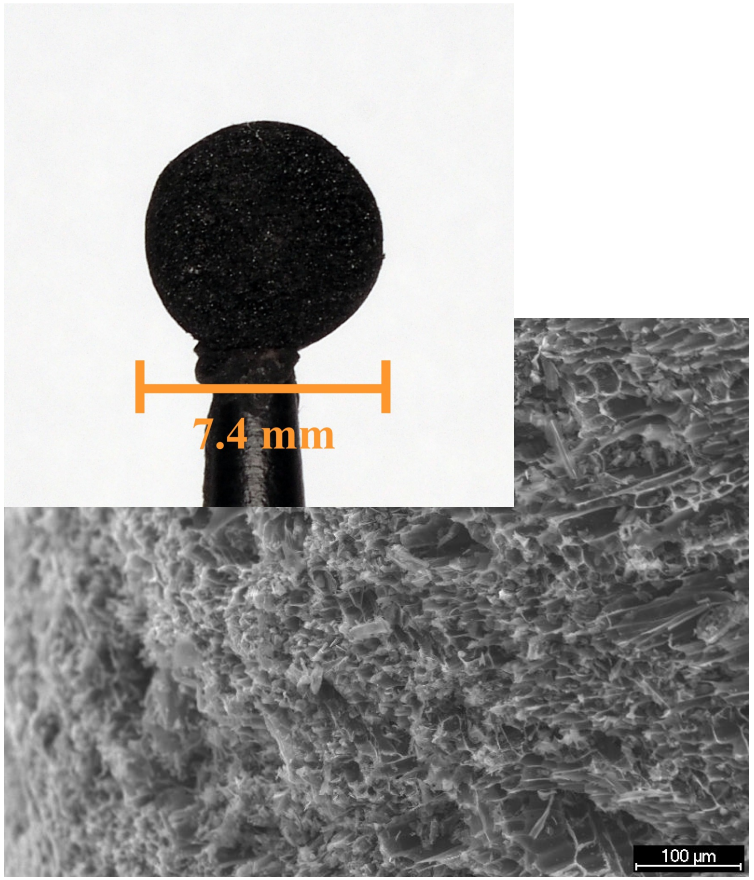

Charcoal

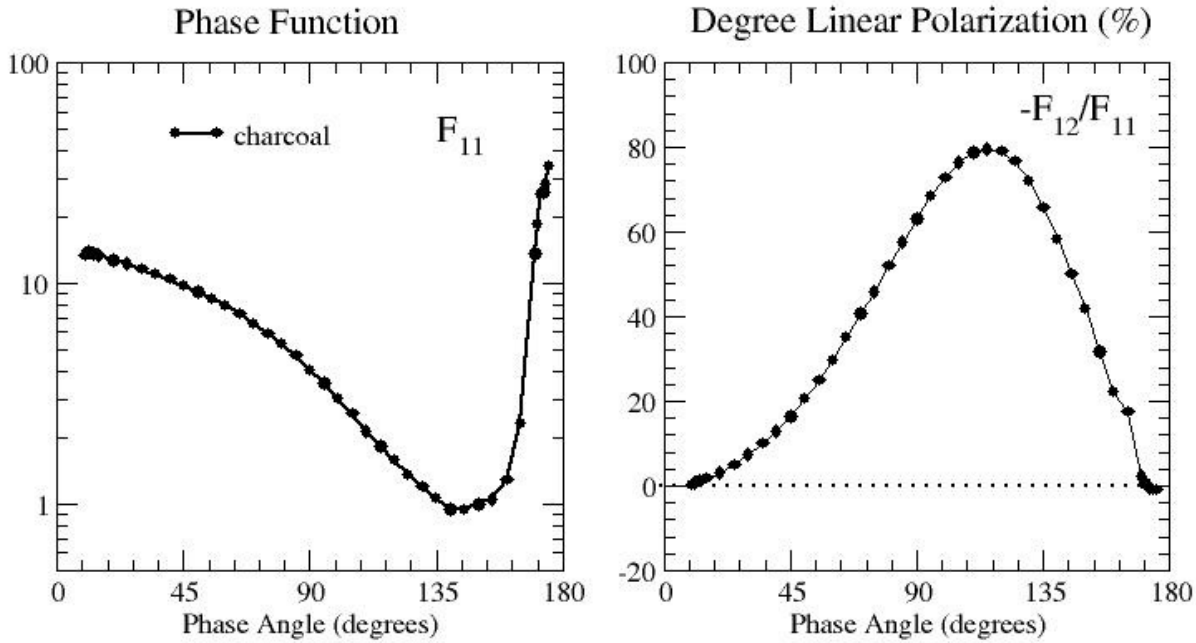

Ray-tracing model, cf., Muinonen et al. (2009), Vuori et al., in press (2024)

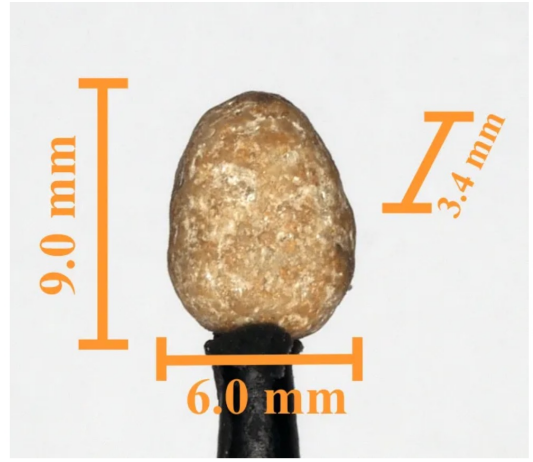
9.0 mm
3.4 mm
6.0 mm

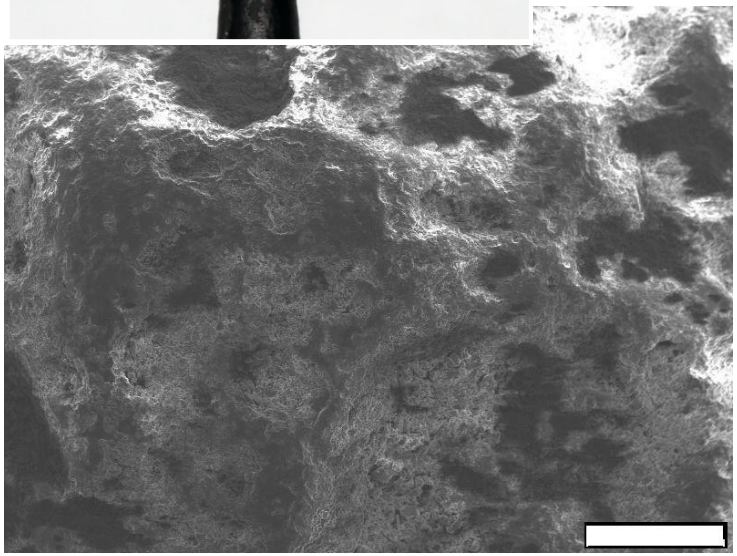

MgFeAlSi

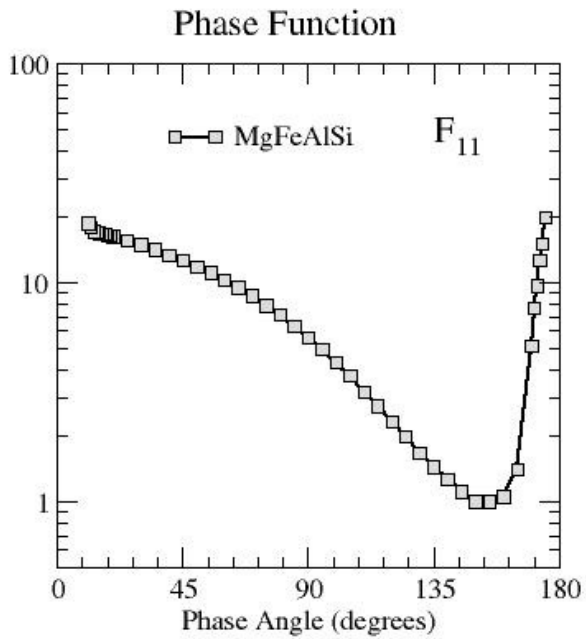
Phase Function
MgFeAlSi
F_{11}
100
10
1
0
45
90
135
180
Phase Angle (degrees)

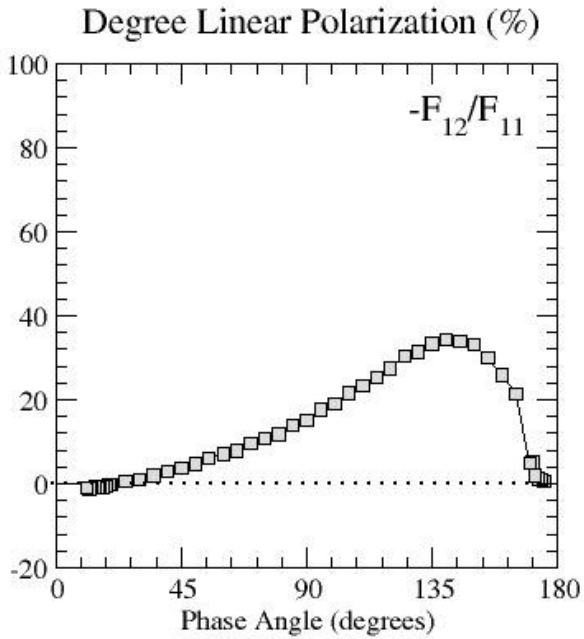
Degree Linear Polarization (%)
$-F_{12}/F_{11}$
100
80
60
40
20
0
-20
0
45
90
135
180
Phase Angle (degrees)

Application: Lunar photometry and polarimetry (1/2)

- Granada-Amsterdam basalt measurements modified for input incoherent scattering matrix (Dabrowska et al. 2015, Muñoz et al. 2012)
- Single-scattering albedo tuned to ω=0.723 to result in lunar geometric albedo of p=0.136
- Mean-free-path length tuned to *kl = 60* to result in correct photometric and polarimetric opposition surges
- Spline representation of input $-P_{12}/P_{11}$ tuned to result in a match with the observed polarization for the waxing (increasing) Moon
- Procedure repeated with approximate and full decomposition of the input scattering matrix for RT-CB

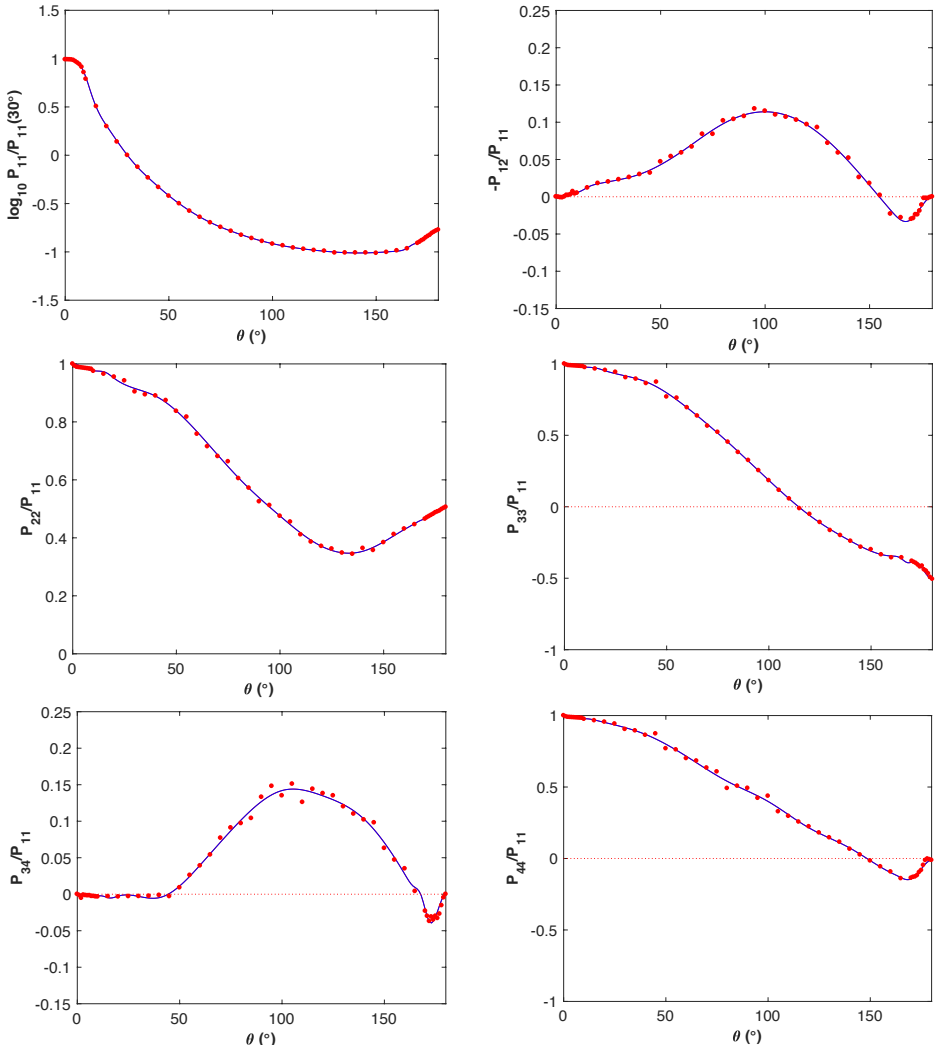

Application: Lunar photometry and polarimetry (2/2)

Approximate scattering matrix decomposition

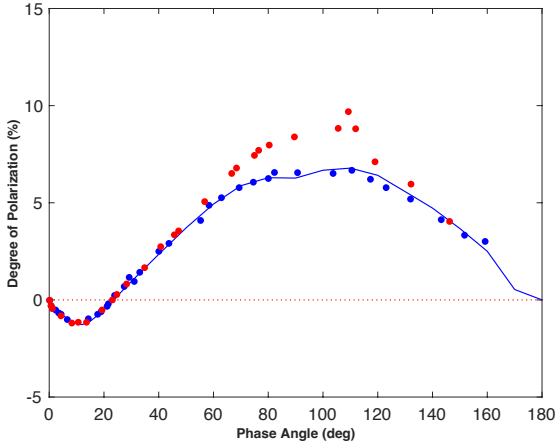

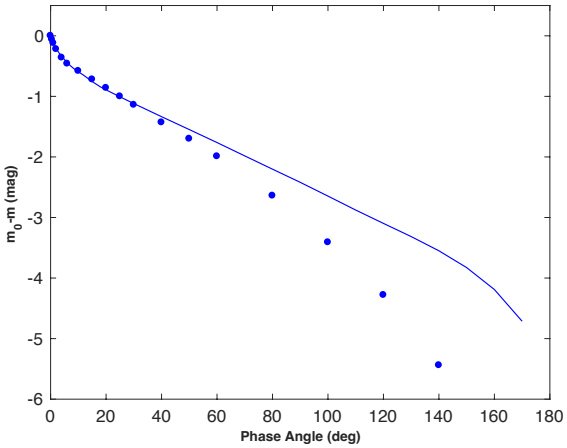

Example single-scattering polarization

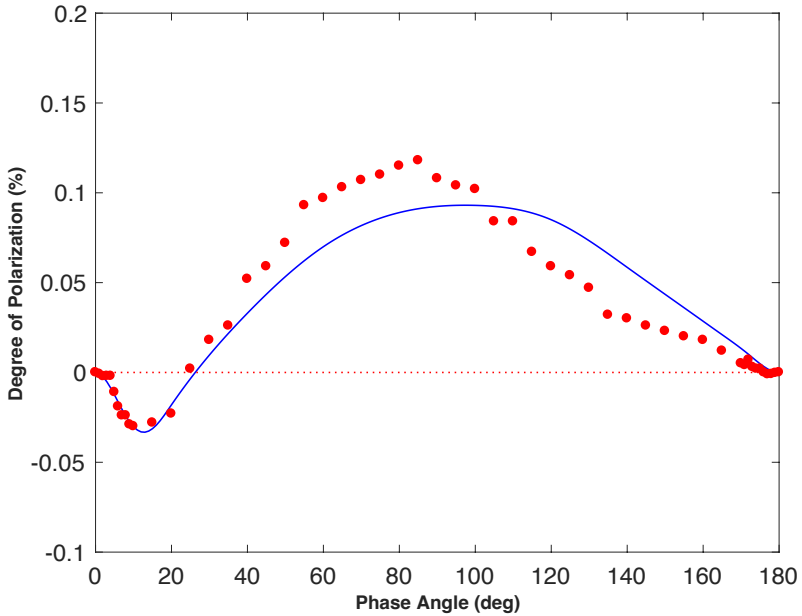

Photometric data from Rougier (1933) averaged by Bowell et al. (1989)
Polarimetric data from Lyot (1929)

Full scattering matrix decomposition

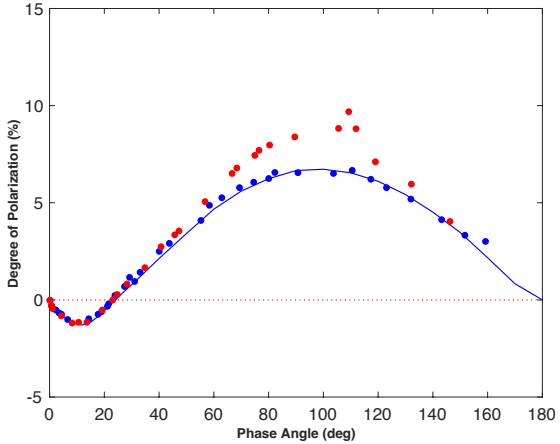

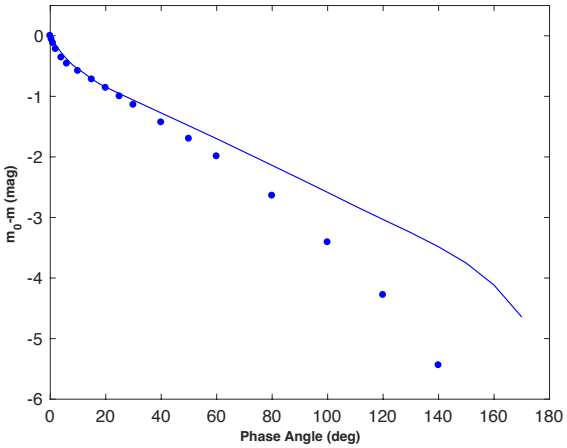

Application: asteroids

Modeling for different taxonomical classes using representative geometric albedos

Muinonen et al.,
in preparation
(obs. ref. therein)

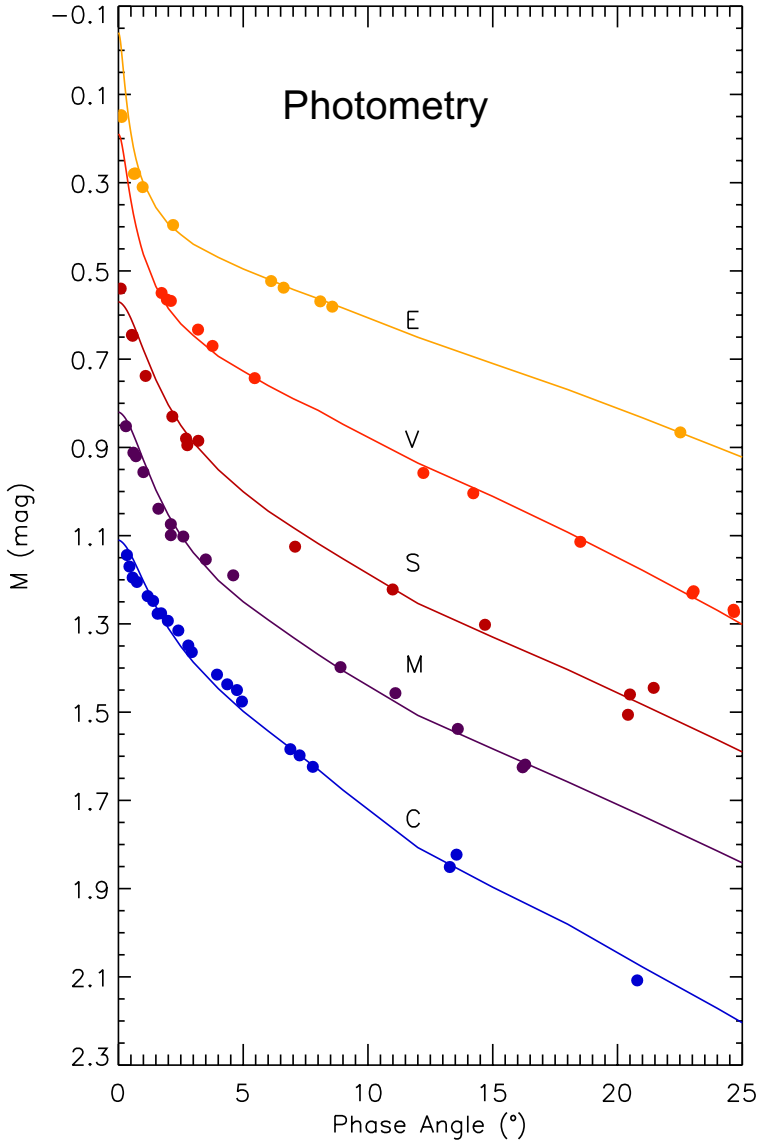

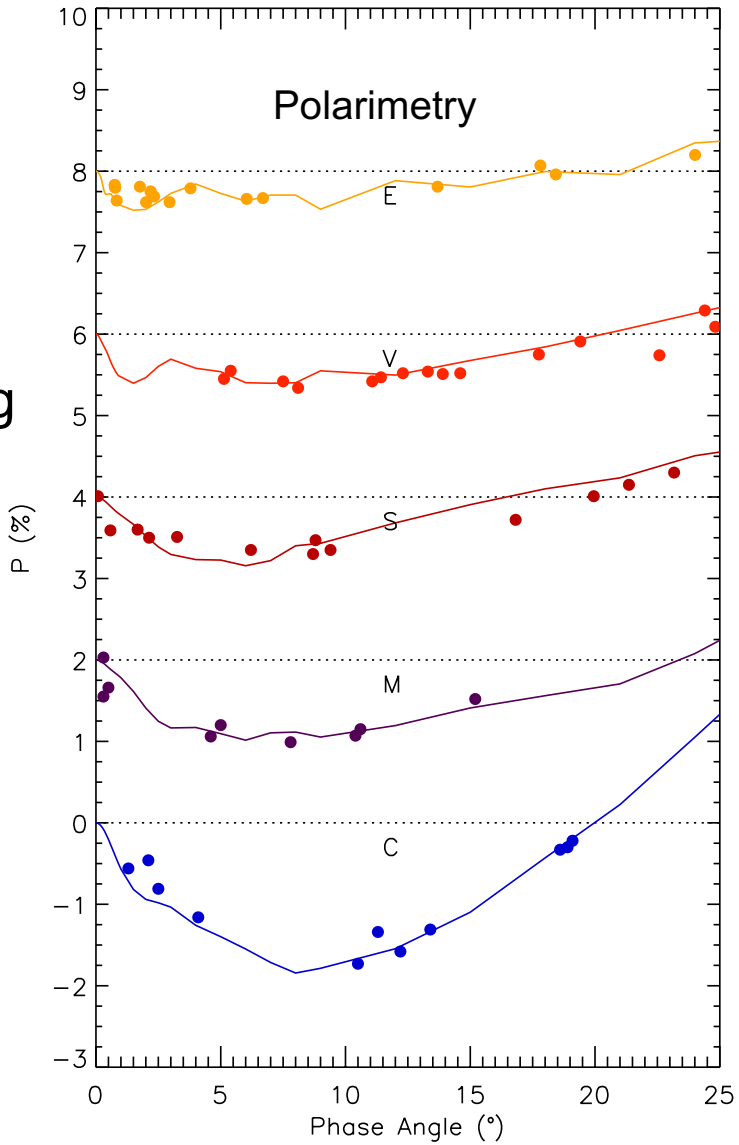

Photometric lightcurve inversion

Apparent, absolute, and reduced magnitudes:

$$
\begin{aligned}
m_{\mathrm{V}}(\alpha) &= H - 2.5\lg\Phi(\alpha) + 5\lg(r\Delta), \\
H &= 2.5(6.259 - 2\lg D - \lg p_{\mathrm{V}}), \\
V(\alpha) &= H - 2.5\lg\Phi(\alpha).
\end{aligned}
$$

Geometric albedo p_V, diameter D, particle single-scattering phase function P_{11}, asteroid phase function Φ, Lommel-Seeliger and particulate-medium reflection coefficients (Muinonen et al., Frontiers Astron. Space Sci. 2022):

$$
\begin{aligned}
R_{\mathrm{PM}}(\mu,\mu_0,\phi) &= 2p\Phi_{11}(\alpha)\Phi_{\mathrm{S}}(\mu,\mu_0,\phi)\frac{1}{\mu+\mu_0}, \\
\Phi_{11} &= \frac{P_{11}(\alpha)}{P_{11}(0^\circ)}, \\
p &= \frac{1}{8}\tilde{\omega}P_{11}(0^\circ), \\
\Phi_{11}(0^\circ) &= 1, \\
\Phi_{\mathrm{S}}(\mu_0,\mu_0,0^\circ) &= 1.
\end{aligned}
\qquad
\begin{aligned}
R_{\mathrm{LS}}(\mu,\mu_0,\phi) &= 2p\frac{\Phi(\alpha)}{\Phi_{\mathrm{LS}}(\alpha)}\frac{1}{\mu+\mu_0}, \\
R_{\mathrm{PM}}(\mu,\mu_0,\phi) &= 2p\frac{\Phi(\alpha)}{\Phi_{\mathrm{PM}}(\alpha)}\Phi_{\mathrm{S}}(\mu,\mu_0,\phi)\frac{1}{\mu+\mu_0},
\end{aligned}
$$

Photometric phase functions from Gaia

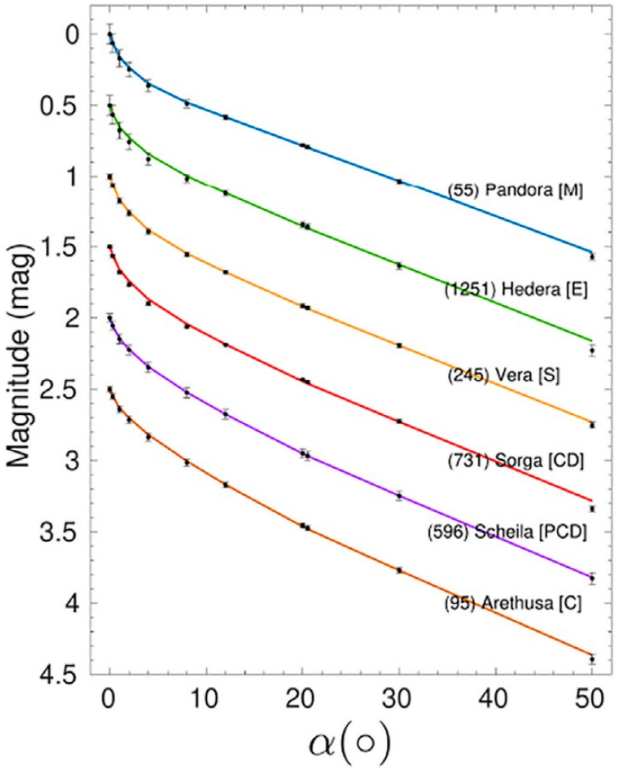

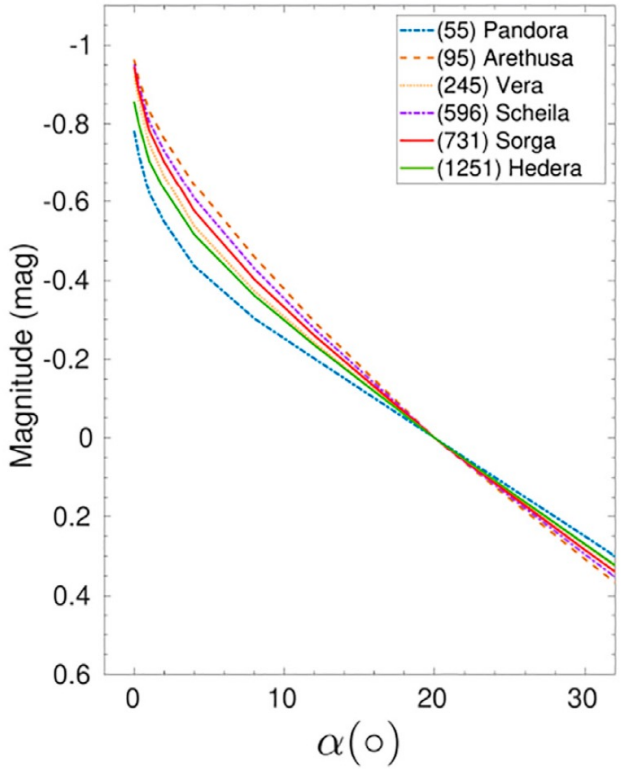

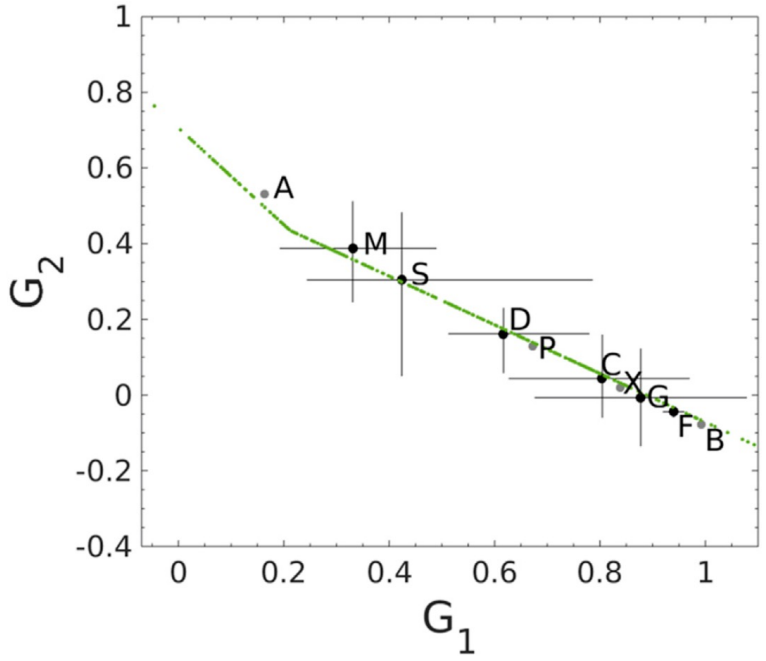

Results from combined Gaia DR2 and ground-based DAMIT photometry using convex inversion, Muinonen et al. (2022) & Martikainen et al. (2021)

Photometric slopes from DR3

MacLennan et al.,
in preparation

Photometric slopes
in mag/rad

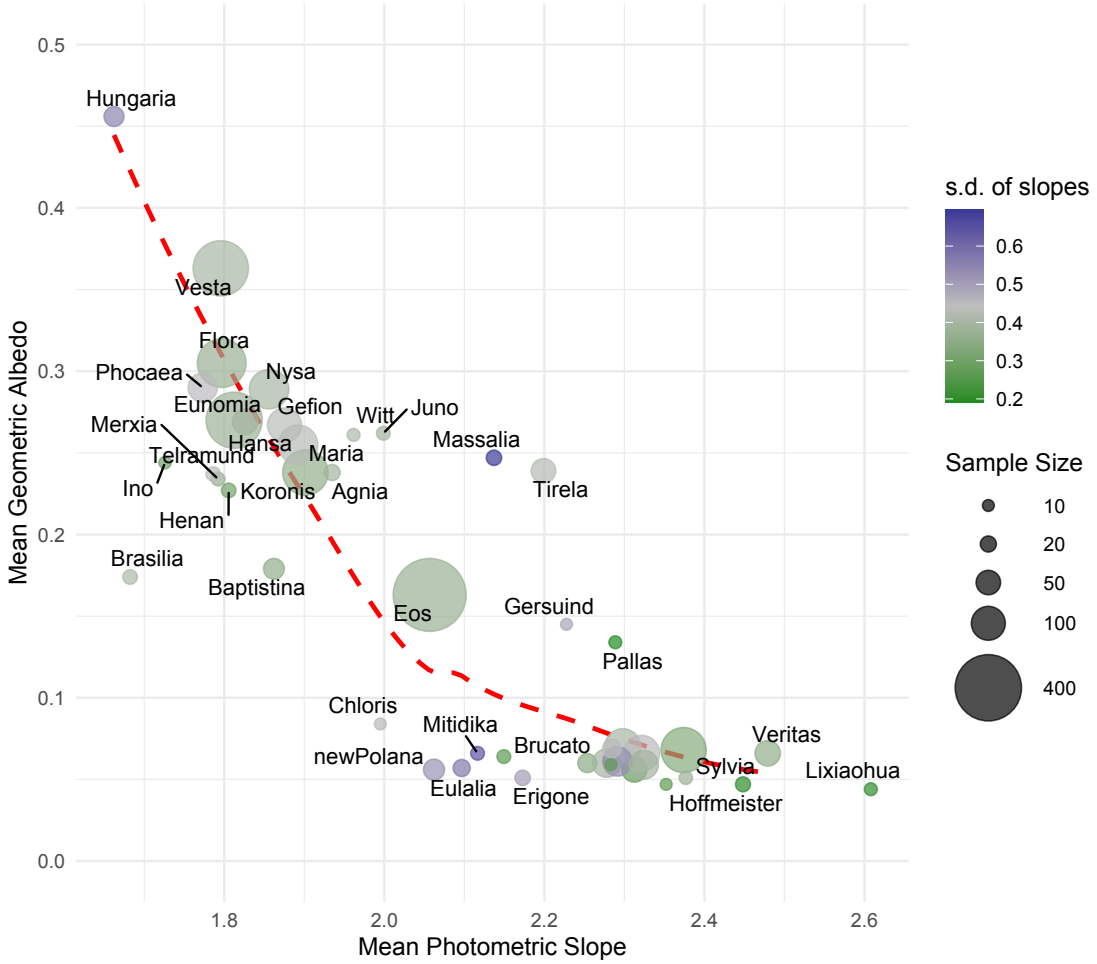

Absolute magnitudes from DR2

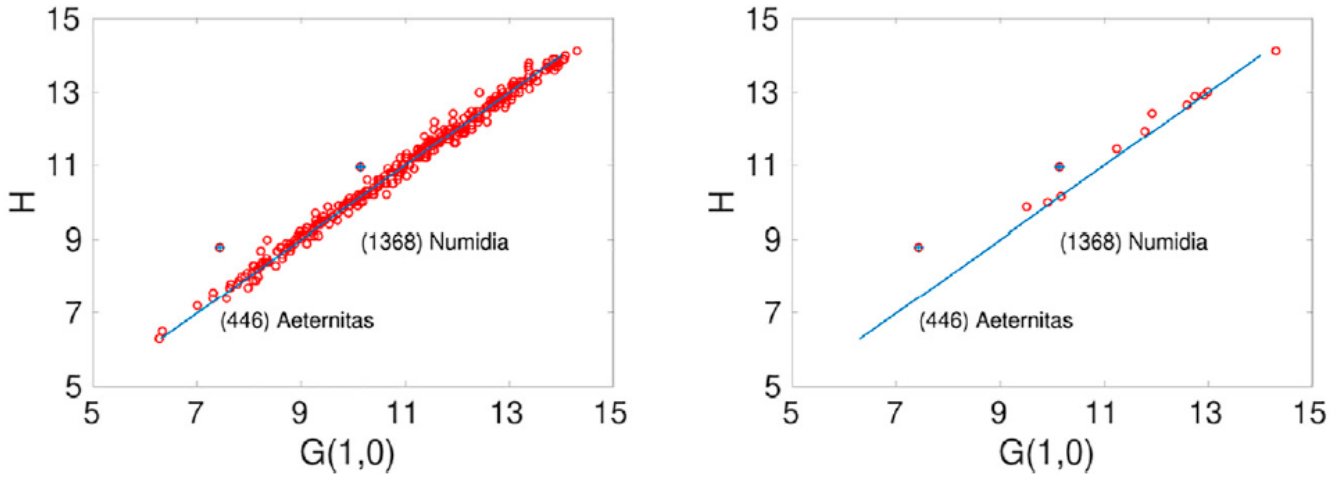

FIGURE 6 | Comparison of the derived equal-sphere G-band absolute magnitudes *G*(1,0) and the V-band absolute magnitudes *H* based on the Jet Propulsion Laboratory Small-Body Database for 358 asteroids (left), the right panel highlighting the 13 new asteroids. The blue line represents perfect correlation of the absolute magnitudes. Two noticeable outliers (446) Aeternitas and (1368) Numidia are marked with blue crosses.

Conclusions with future prospects

- Theoretical modeling and classification, iterative scheme
  - Polarimetric phase function
    - Geometric albedo, regolith scatterers
  - Photometric phase function
    - Regolith roughness, porosity, and scatterers
  - Spectrometry with phase-angle dependency:
    - Regolith composition, roughness, porosity, and scatterers
- Disk-resolved spectrophotometric modeling for Mercury using MESSENGER data
  - Björn et al., in press (PSJ 2024)
- Photometric slopes for *Gaia* asteroids
  - Muinonen et al. (2022); MacLennan et al. (in prep.), and Cellino et al. (2024)
- Color effects near opposition for *ATLAS* asteroids
  - Wilawer et al. (MNRAS 2024)
- Polarimetric and photometric modeling for
  - the Didymos-Dimorphos system (Gray et al., PSJ 2024; Penttilä et al., PSJ 2024)
  - the Galilean satellites Europa, Ganymede, and Io (Kiselev et al., PSJ 2022 and PSJ 2024)